Available online at www.sciencedirect.com

ScienceDirect

Journal of the European Ceramic Society 30 (2010) 2407–2418

www.elsevier.com/locate/jeurceramsoc

A computational analysis of a ZrO_2–SiO_2 scale for a ZrB_2–ZrC–Zr ultrahigh temperature ceramic composite system

Harita Petla[1], Elvia P. Renova[1], Arturo Bronson[*,2], Jack F. Chessa[2], Nischel Maheswaraiah[1]

Department of Mechanical Engineering, University of Texas, El Paso, TX, United States

---

Abstract

The success of a ceramic composite for ultrahigh temperatures (i.e., >1873 K) in an oxidizing atmosphere resides in the protective characteristics of a scale to limit oxygen ingress or to control the oxygen reaction into the substrate. With temperature changes from room temperature to ultrahigh temperatures, the mechanics of the scale and its reactivity becomes critical for ceramic composites to operate under extreme environments. A study was pursued to design computationally a SiO_2–ZrO_2 scale for a ZrB_2/ZrC/Zr–Si composite by using conventional finite element analysis, which was used as a baseline microstructure for the extended finite element method. The model of the Zr boride/carbide composite with a SiO_2/ZrO_2/$ZrSi_x$ scale simulates the development of local strain energetics under a thermal load from 300 to 1700 K. The computational analysis determined that the size of the SiO_2 and $ZrSi_x$ precipitates does not appreciably influence the durability of the microstructure. A simulated annealing optimization algorithm was also developed for an extended finite element program (called XMicro) with the purpose of optimizing the auto re-meshing of XMicro and thus minimizing its combinatorial selection of a composite's reinforcement architecture. After correcting for the overlapping of ZrO_2 precipitates within a matrix, XMicro determined that 1.96 μm as the optimal spacing of precipitates within a cluster and 20 μm between clusters within a silica matrix of the scale interphase. The strategic experimentation determined that porosity developed during oxidation should be incorporated into the simulation of a ceramic composite. To probe into the efficacy of the silica layer for the scale, oxidizing experiments were performed at 1973 K, as well as microstructural analysis of the scale interphase. The computational mechanics coupled with consideration of the thermodynamic stability of phases for the Zr–Si–O system to set the oxygen potentials between layers can design a scale interphase for an ultrahigh-temperature, ceramic composite system. The processing challenge would be to attain the optimal configuration of the microstructure, for example, silicide precipitates developed with the appropriate spacing along a scale/matrix interface or ZrO_2 clusters within a silicate phase.

Keywords: Computational mechanics; Oxidation; Thermodynamics; Phase equilibria; Ceramic composite

---

1. Introduction

In considering the computational modeling of the deformation of ultrahigh-temperature ceramic composites, the effects of crystal structure, elastic anisotropy, grain-boundary sliding and even slow crack growth on the strength of the composite are required. An understanding of the controlling mechanisms is critical especially when extrapolating from the available mechanical properties to predict the ultrahigh-temperature behavior, so a reasoning of the major parameters used are summarized here. The focus of the study was to model the mechanics and thermodynamic stability of a ZrO_2–SiO_2 scale developed on a ZrB_2–ZrC–Zr ceramic composite considering a thermal load from 300 to 1973 K with subsequent cooling. An assessment of the simulations becomes problematic because of limited strain and stress data, so the emphasis was to optimize the scale microstructure confirmed with a few experiments. Though the computational modeling evaluates the durability of the oxide scale from room temperature, the paper will direct its analysis of the oxide scale at temperatures greater than 1000 °C for which less data are available. For the deformation of ceramics at temperatures less than 1000 °C, the reader is referred to the critical reviews of Rice[1] on oxides, and the monograph by Wachtman[2] on ceramics.

1.1. Mechanics of the scale

The strength of ZrB_2 approximates 1.5 times better than ZrC at 1800 K, as determined by researchers[3–8] and comparatively

---

[*] Corresponding author. Tel.: +1 915 747 6931; fax: +1 915 747 5019.
E-mail address: abronson@utep.edu (A. Bronson).

[1] These authors are graduate students in the Department of Mechanical Engineering at the University of Texas at El Paso.

[2] These authors are Professor and Associate Professor, respectively, in the Department of Mechanical Engineering at the University of Texas at El Paso.

0955-2219/$ – see front matter © 2010 Elsevier Ltd. All rights reserved.
doi:10.1016/j.jeurceramsoc.2010.02.027

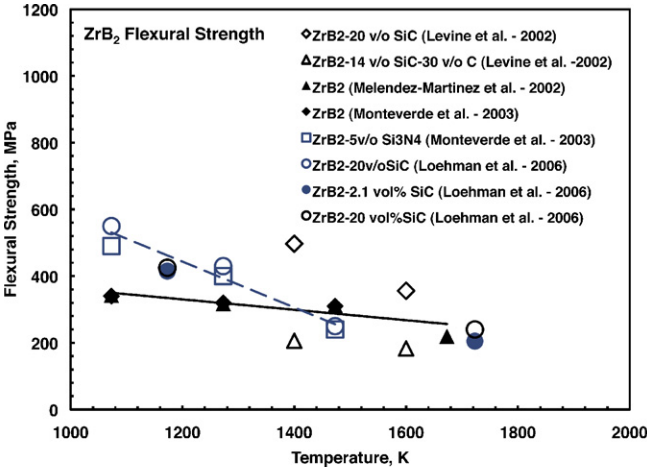

Fig. 1. The flexural strength of ZrB$_2$ used for the simulations of the ZrB$_2$/ZrC/Zr composite.

shown in Figs. 1 and 2. The flexural strength of ZrB$_2$ slightly decreases from 351 to 342 MPa at 298 to 1073 K, respectively, with more dramatic lowering of its strength to 219 MPa at 1673 K. The Si_3N_4 and SiC additions seem to increase the flexural strength at temperatures less than 1300 °C, though the strength of the ZrB$_2$ appear to extrapolate toward higher values than those attained by ZrB$_2$ with either Si_3N_4 or SiC beyond 1500 K. For ZrC, Gridneva et al.[7] determined the flexural strength, but it is significantly less than the compressive yield stress as reported by Darolia and Archbold.[8]

The mechanics of a ZrO_2–SiO_2 scale was considered for simulation, because of its successful protective characteristics on a ZrB_2–SiC composite, as reported by Levine et al.,[3] Hinze et al.,[9] Opeka et al.,[10] and Rezaie et al.[11] The scale consists of a dual layer interphase with an outer SiO_2 amorphous layer covering primarily a ZrO_2 layer with SiO_2 located within the grain boundaries at temperatures greater than 1773 K. Although a B_2O_3–SiO_2 liquid forms because of the eutectic temperature of 372 °C at 67 mol% B_2O_3,[12] boria vaporizes as the composite temperature rises to 1973 K. For example, a ZrB_2–30 vol% SiC mixture as investigated by Rezaie et al. becomes a 61 B_2O_3–39 SiO_2 (in mol%) composition assuming the ZrB_2–SiC reacts stoichiometrically upon oxidation. As the silicate liquid covers the surface and seals pores or grain boundaries, the silicate serves as an effective diffusion barrier to oxygen diffusion. Karlsdottir and Halloran[13] more recently have reported the outer layer as a B_2O_3–SiO_2–ZrO_2 liquid with ZrO_2 precipitates. A key success to the protective borate–silicate scale from room temperature to 1973 K would be the molten phase covering a reactive boride–carbide substrate.

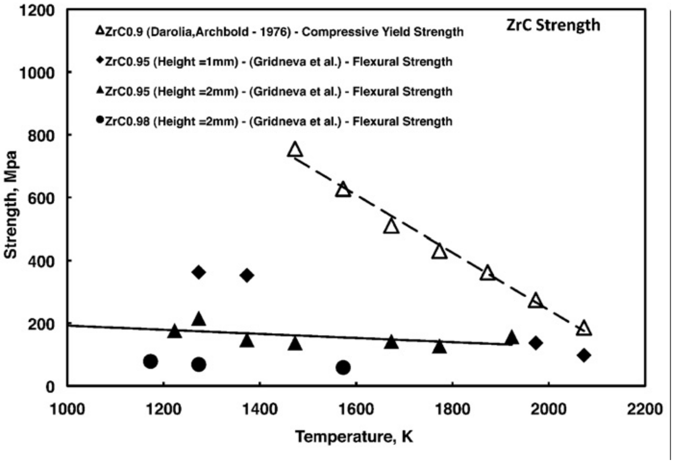

Fig. 2. The flexural strength of ZrC used for the simulations of the ZrB$_2$/ZrC/Zr composite.

For the simulation of the ZrO_2 and SiO_2 within the scale, the mechanical properties for each phase were used, though its mechanics would depend on essentially three regions when considering the phase equilibria of the ZrO_2–SiO_2 system according to Muan.[14] From room temperature to 1950 K, the zircon phase ($ZrO_2 \cdot SiO_2$) is stable until it incongruently transforms to ZrO_2 and SiO_2 phases, but the two-phase field only exists until 1960 K (1687 °C) where eutectic melting occurs at 5 wt% SiO_2. At temperatures greater than 1687 °C, liquid silica would equilibrate with the ZrO_2 phase as expected from the phase diagram. In addition, with impurities collecting in the grain boundaries, the SiO_2 phase would probably melt below its melting point of 1723 °C, which is usually reported for phase diagrams containing silica,[14] or the recent calculated melting temperature of 1725 °C according to Schnurre et al.[15] The flexural strength of SiO_2 steadily increases from 70 MPa at 300 K to 95 MPa at 2000 K according to Borodai.[16]

The flexural strength and elastic modulus of ZrO_2–6.5 mol% Y_2O_3, as reported by Adams et al.[17] was reviewed to determine the possible deformation mechanisms of a ZrO_2 layer of the scale. Rice noted the similar behavior of ZrO_2–MgO and ZrO_2–Y_2O_3 in that the fracture modes are primarily transgranular at 300 K and intergranular at temperatures beyond 1773 K with mixed transgranular and intergranular at 1273 K. Although the flexural strength for sintered ZrO_2–Y_2O_3 of Rice et al.[1] plateaus from 1000 to 1500 °C, the intergranular fracture mode agrees that grain-boundary sliding controls creep of ZrO_2–Y_2O_3, even achieving superplasticity, at temperatures beyond 1273 K as reported by Rice,[1] Jiménez-Melendo et al.[18] Jiménez-Melendo and Domínguez-Rodríguez[19] (hereafter JM–DR)]. A debate ensues on whether an interface-reaction process develops as proposed by Owen and Chokshi,[20] a modified Coble mechanism as suggested by Berbon and Langdon[21] or grain-boundary sliding controls superplasticity for ZrO_2–Y_2O_3 according to JM–DR. An extensive analysis by JM–DR provides a compelling explanation for the segregation of yttrium at the grain boundary affecting deformation, even with impurity or minor addition levels of SiO_2. For a tetragonal ZrO_2–Y_2O_3–5 wt%SiO_2, Kajihara et al.[22] reported that deformation at 1500 °C occurs via a grain-boundary sliding with the silicate phase accommodating the stresses. Hence, the data needed for 1700 °C was extrapolated from ZrO_2–Y_2O_3 considering that grain-boundary sliding would control the deformation, as suggested by JM–DR. As a further consequence, the computational model would consist of a ZrO_2 layer with the SiO_2 phase located primarily within the grain boundaries with minimal reaction between phases.

A comparison of the hot-pressed and sintered zirconia as reported by Adams et al. are shown in Fig. 3. The properties

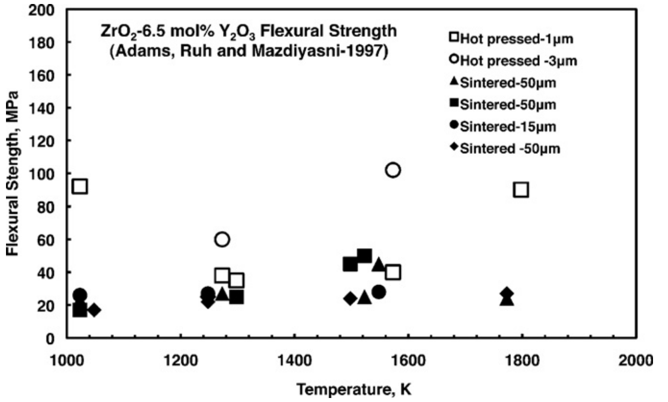

Fig. 3. The flexural strength of ZrO_2 used for the simulations of the $ZrB_2/ZrC/Zr$ composite.

for a sintered rather than a hot-pressed structure were selected for modeling, because the growth of the ZrO_2 layer on a scale would develop without any external stresses.

In the computational approach we are looking at the local strain energy as the quantity we wish to minimize. This is normalized in the phases by the flexural strength strain energy (flexural stress times the strain) of the phase to give a method of comparison between the phases. We do not explicitly consider fracture since we are looking for microstructures that minimize the damage energetics. The foregoing synopsis provides only part of the material properties (including the elastic moduli, coefficients of thermal expansion, and Poisson's ratio) used in the modeling of the scale mechanics with the thermal properties (e.g., thermal conductivity, specific heat capacity), as well as density, for the components of the composites. The experimental data are considerable and the reader is referred to Petla[23] for further study of the data.

1.2. Reactivity of the scale

The growth of the scale would be controlled primarily by the diffusion of the oxygen limited by the boundary conditions of the gas phase and the scale/matrix interface as similarly observed for scales on metals, according to the parabolic rate law. The established scale development has been classically explained by Wagnerian oxidizing behavior[24] by the following equation

$$\frac{1}{A}\frac{d\tilde{n}}{dt} = \frac{1}{\xi}\left[\frac{\tilde{c}}{2}\int_{p_{O_2}^{(i)}}^{p_{O_2}^{(o)}}\left(\left(\frac{Z_M}{Z_O}\right)D_M + D_O\right)d\ln p_{O_2}\right] = \frac{\tilde{k}}{\xi} \qquad (1)$$

The foregoing equation considers the rate of equivalents (ñ) migrating per area (A) across an oxide thickness (ξ) with the self-diffusion coefficient of oxygen (D_O) and cations (D_M) integrated over the oxygen potential (i.e., $d\ln\ p_{O_2}$). Wagner's rational rate constant ($\tilde{k}$) with the units of equivalents/(cm s) is usually converted to the parabolic rate constant (k_p, cm^2/s). For further explanation of Wagner's parabolic rate law, the reader can refer to Wagner,[24] Yurek[25] and Kofstad.[26] The former rate constant with the concentration of equivalents ($\tilde{c}$, equivalents/cm^3) can be easily converted to k_p (i.e., $\tilde{k}/\tilde{c} = k_p$). The limiting criteria for the integral represents the thermodynamic activities, in this case the oxygen potential at the gas/scale interface ($p_{O_2}^{(o)}$) and the scale/layer interface ($p_{O_2}^{(i)}$). Hence, scale growth of a ceramic composite would depend on the diffusivity of the ionic defects in the zirconia phase (or O_2 within liquid silica) and the oxygen differential (i.e., $d\ln\ p_{O_2}$) with its boundary conditions established by the oxygen potential (i.e., $p_{O_2}^{(o)}$ and $p_{O_2}^{(i)}$) determined usually by the phase equilibria.

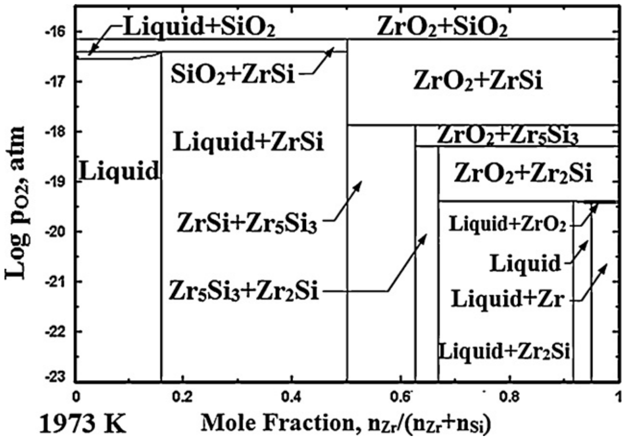

Fig. 4. The Zr–Si–O phase diagram considering the oxygen potential of the coexistence of phases at 1973 K.

Silicide precipitates were also considered as part of the scale interphase on the premise that a three-phase field would establish the oxygen potential and thus control oxygen ingress through the scale. At 1700 °C, the oxygen flux will be controlled by two oxygen potentials – one determined by the gas phase and one fixed by a three-phase field consisting ZrO_2–ZrSi(s)–SiO_2(l). In terms of the Gibbs phase rule for the Zr–Si–O system, the phase assemblage creates a bivariant situation ($F = C - P + 2 = 3 - 3 + 2 = 2$), but with the temperature defined and at atmospheric pressure, the assemblage becomes invariant. A similar fixation of the oxygen potential occurred at 2000 °C for a ZrO_2 phase coexisting with silicide and silicate liquids as reported by Peña et al.[27] In addition to slowing the oxygen transport through silica, Peña et al. reported that the silicide coating survived for more than 49 h, because of the fixation of the oxygen potential.

The effect of the three-phase equilibrium is more easily apparent with a calculated phase diagram depicted according to the Zr mole fraction and the partial pressure of oxygen at 1973 K, as shown in Fig. 4. The horizontal lines actually show constant oxygen potentials such as the ZrO_2–SiO_2–ZrSi equilibrium occurring at the highest oxygen partial pressure ($\log\ p_{O_2} = -16.2$). The next lower oxygen potential with three-phase equilibrium for solid phases corresponds to the ZrSi–Zr_5Si_3–ZrO_2 coexistence at $\log\ p_{O_2} = -17.9$.

The Zr–Si–O phase diagram was calculated via the FactSage database and software (version 6.1),[28] which also incorporated the Scientific Group Thermodata Europe (SGTE) database. However, the Okamoto phase diagram[29] shows the eutectoid temperature for Zr_5Si_3 at 1745 °C (2018 K); the SGTE database gives it at 1433 °C (1806 K). In addition, the Okamoto phase diagram does not show the $Zr_5Si_3 + ZrSi$ phase-field bounded by the following SGTE eutectic reaction at 2407 °C (2680 K) and the peritectoid reaction at 1660 °C (1933 K), respectively:

$$\text{Liquid} = Zr_5Si_3 + ZrSi \tag{2}$$

$$Zr_5Si_3 + 5ZrSi = 2Zr_5Si_4 \tag{3}$$

Further analysis of the differences in phase equilibria is needed for temperatures greater than 1973 K, especially 2680 K, but these temperatures are not the focus of the present evaluation.

Although three-phase equilibrium within the scale interphase would decrease oxygen ingress as established by the Wagnerian rate law (Eq. (1)), the effect of silicide-precipitate size on the strain energetics within the scale interphase should also be considered. The scale must also withstand subsequent temperature cycling causing dramatic changes in the strain distribution along the interphase. In the present study, the local strain energetics was used to infer an optimal scale configuration knowing that it is an initial step in understanding oxidation at extreme temperatures by coupling scale mechanics and reactivity.

A computational approach then validated with strategic experimentation is not new and has recently been applied in designing alumina–carboneous (A–C) and mullite–carboneous (M–C) refractories[30] and ZrB_2 and ZrB_2–30%SiC composites[31] for thermal shock resistance. Finite element models were used to simulate the effect of temperature gradients on the stresses of the composite during a temperature change. For example, the thermal expansion coefficient was higher for an A–C refractory than for a M–C refractory and caused by higher stresses for the former. However, the stresses were offset by a lower temperature gradient for A–C than for M–C because the thermal conductivity was higher for the A–C refractory. For ZrB_2 and ZrB_2–SiC, the thermal shock resistance was determined experimentally as similar. In the finite element analysis of ZrB_2–SiC, Zimmermann et al.[31] reported that the low heat transfer between the SiC particles and the surrounding ZrB_2 matrix caused residual stresses to develop. In both studies, the finite element analyses revealed specific attributes of the interaction between temperature gradients and stresses sometimes not discerned in an experimental study. However, studies coupling the computational mechanics with the computational thermodynamics have been limited, especially at ultrahigh temperatures.

2. Computational approach

2.1. Damage modeling of scale interphase with non-linear finite element analysis

The durability of the ZrO_2–SiO_2 scale on a ZrB_2–ZrC–Zr composite at ultrahigh temperatures was simulated with a mesh generated by Altair HyperMesh for the conventional finite element software of the LS-DYNA code developed by Livermore Software Technology Corporation (LSTC). The mesh was drawn manually with an element size approximating 2 μm with a configuration shown in Fig. 5. The mesh consisted of dual layers of SiO_2 and ZrO_2 as the scale interphase with a thickness of 50 and 80 μm, respectively, for a ZrB_2–ZrC–Zr substrate, as shown in Fig. 5. Silicide precipitates were embedded within the zirconia layer near the ZrO_2/matrix interface to complete the baseline mesh of the ZrO_2–SiO_2 scale on a ZrB_2–ZrC–Zr matrix or substrate.

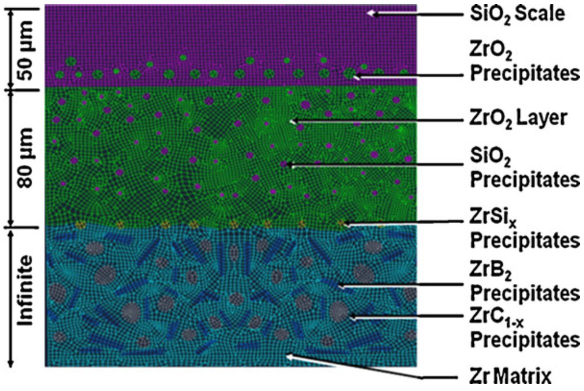

Fig. 5. The baseline mesh used for conventional finite element analysis considering a dual layer of SiO_2 and ZrO_2 layer protecting an underlying ZrB2/ZrC/Zr composite.

The thermal load onto the scale/substrate was applied with a temperature rise from 300 to 1973 K within a hour, an isothermal hold for 6 h at 1973 K followed by an expected convective cooling of a solid, as shown in Fig. 6. The temperature cycle was selected according to the usual oxidizing studies. An adiabatic process was assumed after simulating two scenarios–one with temperature defined at the surface with heat conduction developing inwardly to the substrate and another case in which the temperature was defined for all the nodes. The strain and stress had no significant difference for both cases with a scale thickness totaling 130 μm.

Physical, mechanical and thermal properties of each of the phases depicted in the baseline mesh required for the code were: density, Young's modulus, Poisson's ratio, yield stress, coefficient of thermal expansion, thermal conductivity and specific heat capacity, as available by Petla.[23] The mechanical properties at ultrahigh temperatures are sparse so assumptions were made in most cases by extrapolating properties at the available temperatures or substituting for related parameters (e.g., flexural strength for yield stress). One must be aware sometimes of the complicated relationship between flexural and tensile stress, as Marshall and Evans[32] have reported. As an example of a parameter assumption, the elastic modulus for ZrB_2 was con-

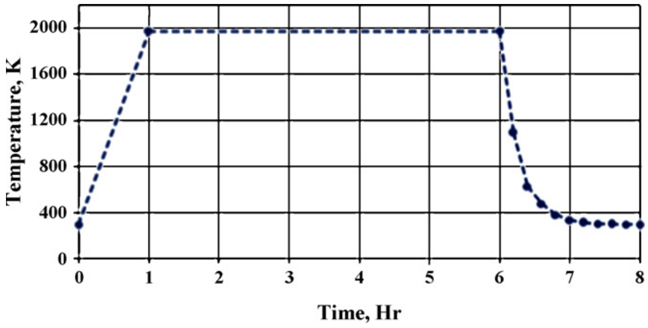

Fig. 6. The thermal cycle used to load the composite for the simulations.

Table 1
Elastic moduli of components used for modeling.

Material	Density (g/cm^3)	Elastic modulus (GPa)						
		Temperature (°C)						
		20	200	500	800	1100	1400	1700
ZrO_2	5.62	222	213	178.5	179	178	169	160.5
ZrB_2	5.28	346	346	346	346	346	346	346
ZrC	6.605	390.3	387.4	379.5	368.7	358.9	344.2	326.6
SiO_2	2.21	72.4	73.5	75.6	77.9	79.4	80.4	81.6
Zr	6.49	106	94	74	54	24.42	24.42	24.42
Ti_5Si_3	4.32	156	155	153	145	142.2	137.7	133.2
ZrB_2/ZrC/Zr	6.2	286	253	199	145	64	64	64

sidered unchanged because of its crystal structure and strength behavior with increasing temperature (Fig. 1). In addition, the elastic modulus of ZrB_2 is reasonable when the elastic moduli of the components do not vary significantly, especially ZrC, as shown in Table 1. For the coefficient of thermal expansion, the individual components of the components were used as shown in Table 2. For more information, the reader is referred to Petla who has summarized the parameters for the mechanical and thermal properties of the components.

The yield stress of zirconium disilicide is available but with a melting point of 1620 °C (or 1893 K), its usage requires a small extrapolation to 1973 K. The four silicides (e.g., ZrSi, Zr_5Si_4, Zr_3Si_2, Zr_5Si_3 and Zr_2Si) located in the middle of the Zr–Si phase diagram are stable at 1973 K, though their yield stress or flexural strengths were not found after an extensive search in the literature. Umakoshi et al.[33] have determined the yield stress for a Ti_5Si_3 single crystal, which was considered a valid substituting constituent for the Zr silicide because of titanium's proximity to Zr on the periodic table. Although the multivalency of Ti differs from Zr, the Zr_5Si_3 phase with the same hexagonal structure of Ti_5Si_3 has a similar fracture toughness determined through microindentation as Ti_5Si_3 according to Ikarashi et al.[34]. Hence, the data for the yield strength of Ti_5Si_3 acquired by Frommeyer and Rosenkranz[35] were used for the simulations after comparing results from researchers[33–37] because of the wider temperature range, as shown in Fig. 7.

Table 2
Coefficients of thermal expansion of components used for modeling.

Material	Coefficient of thermal expansion, 10^6/(K)						
	Temperature (°C)						
	20	200	500	800	1100	1400	1700
ZrO_2	8.8	9.8	10.6	11.21	12.1	13.01	13.91
ZrB_2	6.7	6.7	6.89	7.11	7.34	7.56	7.79
ZrC	5.6	5.6	5.9	6.6	7	7.2	7.3
SiO_2	0.51	0.57	0.58	0.52	0.51	0.51	0.51
Zr	5.74	5.98	6.47	7.1	6.3	7.57	8.86
Ti_5Si_3	6.7	7.3	8.25	8.5	8.77	9.16	9.7
ZrB_2/ZrC/Zr	6.6	6.6	6.8	6.9	7.1	7.1	7.1

2.2. *Strain modeling of SiO_2–ZrO_2 layer with extended finite element analysis*

The extended finite element or enriched method predicts the strain and stress distribution along discontinuities such as inclusions or cracks without remeshing the microstructure as reported by Sukumar et al.[38] The enriched method consists of adding functions to the scaler variable $u(x)$ whereby only the elements near the discontinuities, such as ZrO_2 precipitates in a silica layer in the present study, are enriched. The additional function for interface discontinuities is the absolute value $f_a(X)$, which is the level set function or the signed distance from any point normal from the ZrO_2 precipitate and a_i is the unknown scalar variable of a node in the enrichment zone simulated as reported by Belytschko et al.[39]

$$u(x) = \sum_{1} N_i(x)(u_i + a_i|f_a(x)|) \tag{4}$$

whereas, the formula for a continuous surface is only

$$u(x) = \sum_{1} N_i(x)(u_i) \tag{5}$$

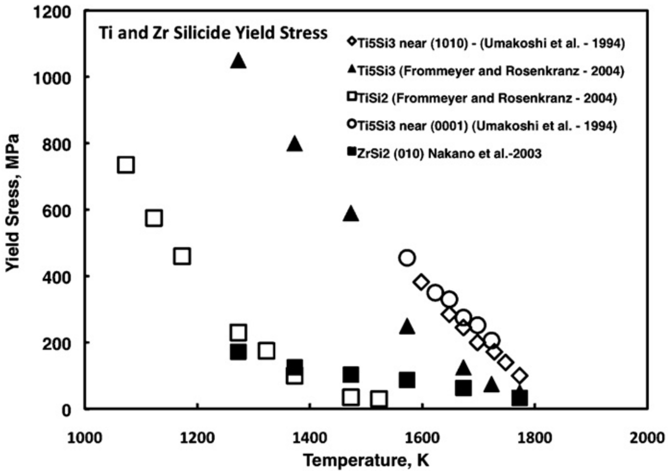

Fig. 7. The yield strength of silicides used for the simulations of the ZrB_2/ZrC/Zr composite.

Table 3
Properties of SiO_2 and ZrO_2 constituents.

Material	Young's modulus (GPa)	Poisson's ratio	Density (kg/m^3)	Coefficient of thermal expansion, $10^6/(K)$
Silica	74.0	0.17	2200	0.6
Zirconia	186	0.33	6040	8.2

for which N_i represents the finite element method for regular shape functions.

An extended finite element code, named XMicro, was developed to compute the thermal stresses on standard elements by considering the initial strain resulting from a temperature rise. The linear elastic plane strain (ε) is:

$$\varepsilon = B^T d \tag{6}$$

where B is the nodal sub-matrix and d is the displacement matrix. The strain energy at each node is then calculated as an objective function,

$$U_t = \sigma_{11}\varepsilon_{11} + \sigma_{22}\varepsilon_{22} + 2 * \sigma_{12}\varepsilon_{12} \tag{7}$$

where σ is the stress of the element.

The simulations using XMicro consisted of ZrO_2 precipitates embedded in a silica matrix. Although the regular finite element analysis considered a thermal load of 300–1973 K, the extended finite element analysis considered a reference temperature of 573–1073 K with the mechanical and physical properties shown in Table 3. For optimization purposes, the range of the volume fraction was restricted to 10–50% of ZrO_2 with their number restricted to 16. The aspect ratio ranged from 0.1 to 10 with the former representing a horizontal ZrO_2 precipitate within a silica matrix and the latter is a vertical precipitate. The domain of the SiO_2 matrix was fixed at a 900 μm^2 grid meshed with 0.25 μm sized triangular elements.

3. Experimental approach

To validate the modeling, a composite of ZrB_2/ZrC/Zr–Si was formed by infiltrating molten Zr–Si (2.1 g) into a packed bed of B_4C particles (i.e., <10 μm diameter and 0.25 g) contained in a carbon crucible heated to approximately 2200 °C with an induction furnace shown in Fig. 8. The process extends essentially the technique developed by Johnson et al.[40] who originally reacted liquid Zr with B_4C particulates at 1900 °C to acquire a pore free composite of ZrB_2/ZrC/Zr. The liquid Zr reacts with the carbide according to the following exothermic reaction:

$$3Zr + B_4C \rightarrow 2ZrB_2 + ZrC \tag{8}$$

Although a stoichiometric reaction is shown, an excess amount of Zr can be used to serve as a matrix containing the boride and carbide. Johnson et al.[40] also infer that the temperature of the Zr/B_4C interface may reach 2300–2400 °C even though the furnace temperature was set at 1900 °C. In the present study, the molten Zr serves as the carrier for the Si with the expectation of developing a ZrO_2–SiO_2 scale on the composite.

Samples were oxidized in a $MoSi_2$ furnace at 1700 °C in air. The temperature of the samples was raised to 1700 °C in 4 h, maintained at 1700 °C for 44 or 48 h and decreased to room temperature in approximately 4 h. A ZrB_2/ZrC/Zr–Si composite was simply placed on a zirconia refractory pedestal then heated to temperature. A Pt/Pt–10 wt%Rh thermocouple placed adjacent to sample was used to check the furnace temperature, which was controlled with a Pt–20 wt%Rh/Pt–40 wt% Rh thermocouple. The measuring thermocouple was removed intermittently to minimize Pt or Rh vaporization after measuring temperatures at 1100–1600 °C at approximately 100° increments. To ensure the development of a SiO_2 layer, another composite sample (1.2 g) was also placed within a quartz tube (1 cm outside diameter, 8 mm inside diameter), evacuated and sealed with a hydrogen–oxygen torch. The encapsulated composite was then heated to 1700 °C and maintained for 48 h. At approximately 1650 °C, the quartz wall collapsed and surrounded the composite with a SiO_2 layer of 1 mm thickness. To determine the stability of the SiO_2 layer, Zr metal (0.2 g) and $ZrSi_2$ powder (0.3 g) were similarly encapsulated and annealed for 44 h at 1700 °C.

The quartz ampoules were placed on ZrO_2–8 wt% Y_2O_3 chips contained in an alumina crucible and then heated to 1700 °C. The quartz contacted the ZrO_2–Y_2O_3 surfaces to minimize the formation of a Al_2O_3–SiO_2 melt resulting from its eutectic (i.e., 1587 °C), but instead a ZrO_2–SiO_2 melt approximating 97 wt% SiO_2 would stabilize at 1700 °C.

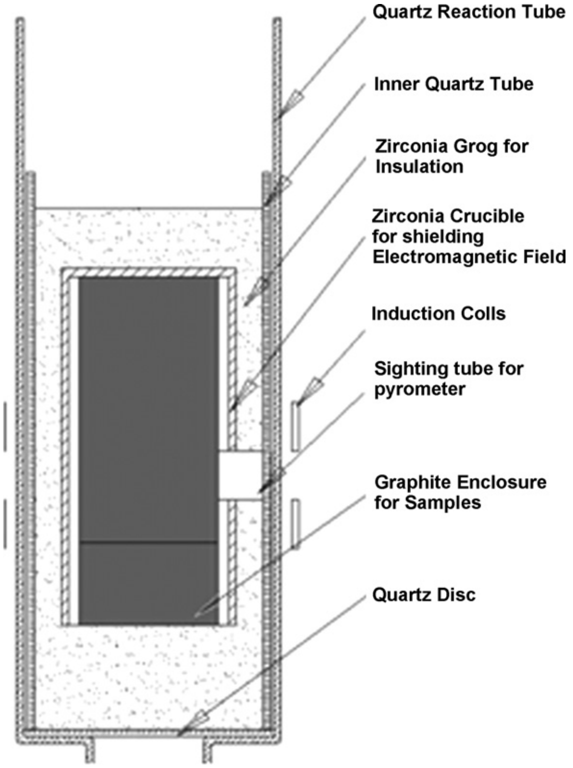

Fig. 8. Experimental setup within induction furnace.

For microstructural characterization, samples were prepared metallographically to a 1 μm diamond polish for examination in a field-emission, scanning electron microscope (Hitachi S-4800). In addition, an energy dispersive X-ray microanalysis (EDAX with Gensis software) provided qualitative elemental analysis, which was augmented with known phase diagrams (e.g., Peña et al.[27] for Zr–Si–O and Okamoto[29] for Zr–Si) to determine the phases within the microstructure.

4. Results

The simulation of the strain for the interphase (depicted in Fig. 5) was calculated via a design of experiments (DOE) factorial study. The number of simulations (N) considered one replica (R), two levels ($L = 2$) of importance of high and low extremes of the effect of parameters or factors ($k = 3$) consisting of ZrB_2 fibers, ZrC precipitates, ZrO_2 precipitates and $ZrSi_x$ precipitates, as summarized in Eq. (9).

$$N - RL^k = 1(2)^3 = 8 \tag{9}$$

The eight simulations amounted to four low levels of the baseline mesh, and for the high level, the parameters were increased by 100%. The ZrB_2 fibers and ZrC precipitates amounted to 20% of the area considered as a low level within the ZrB_2–ZrC–Zr matrix and 30% as the high level. The area of the $ZrSi_x$ precipitates amounted to 17 μm as the low level and 30 μm for a high level simulation.

The eight simulations indicated that the size of the ZrB_2 and ZrC phases contributed significantly to the maximum strain, as shown in Fig. 9. The four simulations with the smaller areas of the boride and carbide precipitates developed lower strains than the four simulations with meshes containing larger precipitates. The effect of the silicide precipitates on the interface strain was apparent in models 1 and 2 in which a larger $ZrSi_x$ area increased the strain when the areas of the ZrB_2, ZrC and ZrO_2 constituents maintained at lower levels. However, the ZrO_2 area or layer did not dramatically influence the calculated strain when considering the eight simulations in either the low or high levels. In addition, the silicide precipitates along the scale/matrix interface did not affect significantly the strain especially when the microstructural areas of the boride and carbide precipitates were at the higher levels. A comparison of the strain distributions for models 4 and 5 indicates that the ZrO_2 layer acquired less strain approximating 0.04 to 0.05 for the former than for the latter (approximating 0.13 to 0.2), as shown in Figs. 10 and 11.

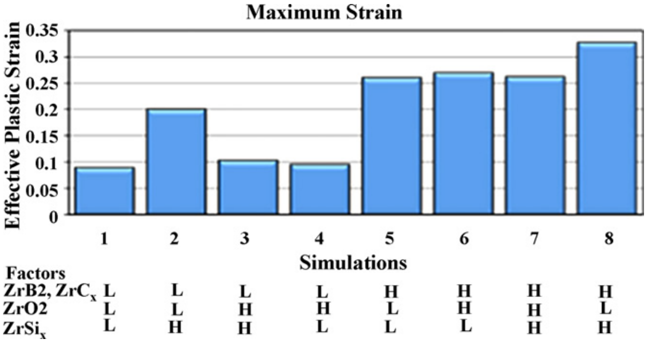

Fig. 9. The maximum strain acquired for high and low configurations of the ZrB2, ZrC and Zr silicides.

For the enriched finite element method, a simulated annealing optimization algorithm was implemented to determine a preferred distribution of ZrO_2 precipitates within the silica layer. To confirm the accuracy of XMicro simulation, the calculated strains for one precipitate within SiO_2 were compared with a regular finite element method using a Hypermesh software, as shown in Fig. 12. The strains determined with XMicro for the x-, y- and xy-direction are within 10% of the strains calculated with Hypermesh indicating an accurate simulation of the enriched finite element method. Then, the strain energies for one and five precipitates randomly distributed were calculated with the minimal standard deviation for which typical results are shown in Fig. 13.

Next, XMicro was used to determine the optimal strain configuration of 16 ZrO_2 precipitates ranging from 10% to 50% within a SiO_2 matrix were successfully calculated with XMicro. The aspect ratio of the ZrO_2 precipitates ranged from 0.1 to 10 with their size varying from 1.8 to 90 μm within a SiO_2 domain of 900 μm. The minimum strain energies corre-

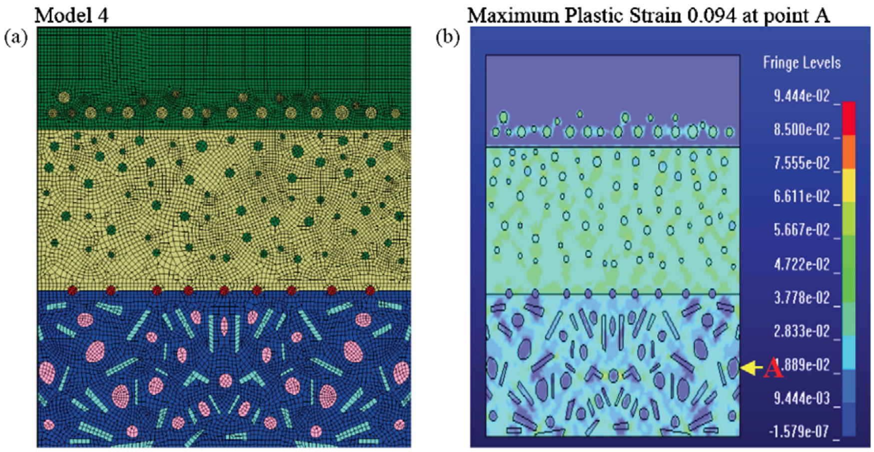

Fig. 10. Strain distribution of low configurations of a ZrB_2/ZrC/Zr composite with (a) showing the mesh and (b) the corresponding strain distribution.

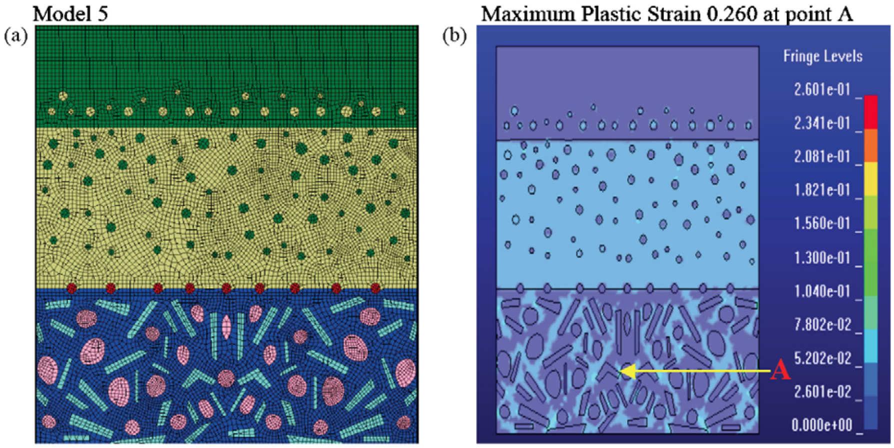

Fig. 11. Strain distribution of high configurations of a ZrB_2/ZrC/Zr composite with (a) showing the mesh and (b) the corresponding strain distribution.

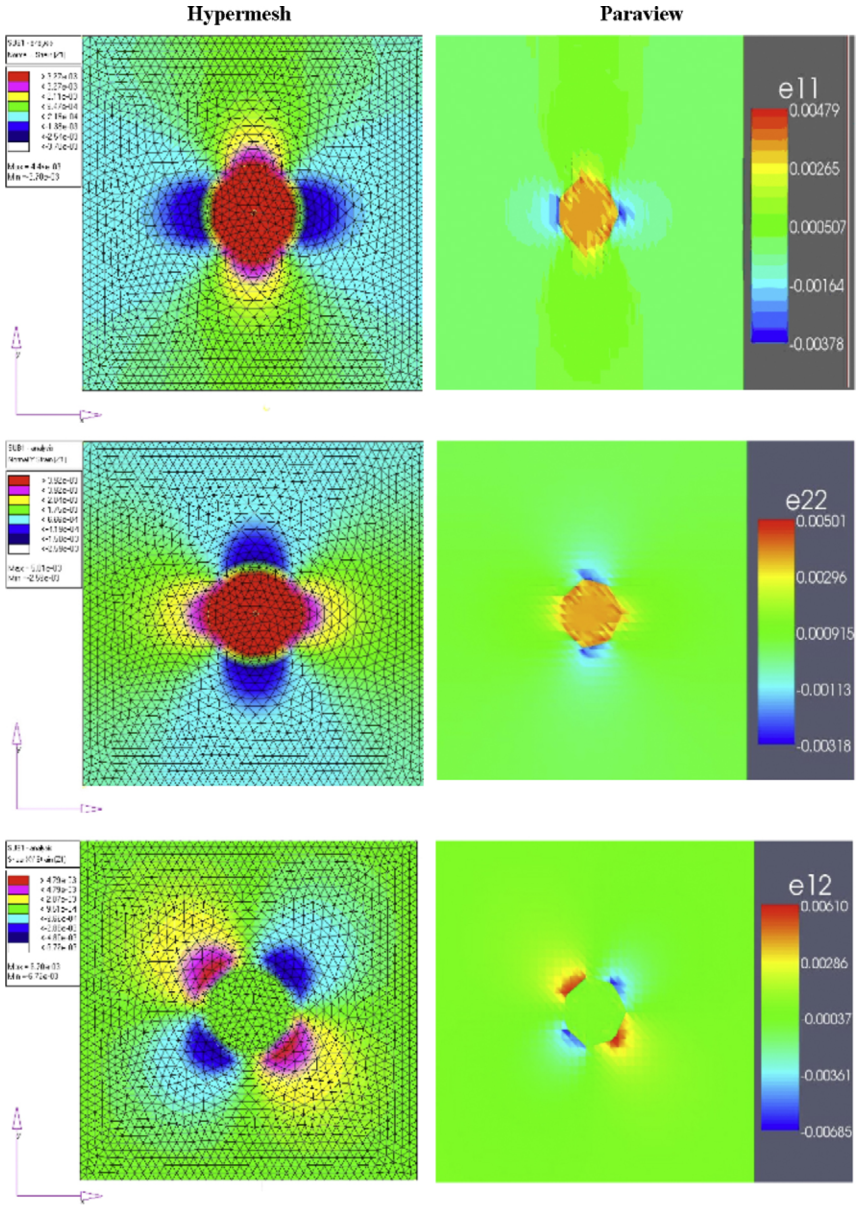

Fig. 12. Comparison of the Hypermesh finite element analysis with an extended finite element method with (a) e11, (b) e22 and (c) e12.

Table 4
Minimum strain energies of SiO_2 constituents within ZrO_2 layer.

Size of precipitates (μm)	Aspect ratio	Area of precipitates (μm)	Volume fraction	Strain energy (GPa/m^3)
1.69	8.56	6.2	0.11	0.0137
1.74	8.34	6.8	0.12	0.0142

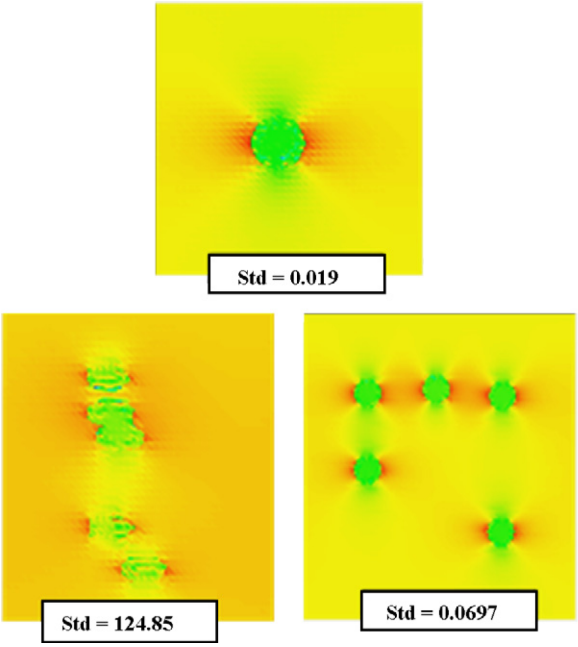

Fig. 13. Random particles distributed among a silica matrix for strain energies with standard deviations of (a) 0.019, (b) 124.85 and 0.0697.

sponded to precipitate sizes of 1.69 and 1.74 μm, as shown in Table 4.

The optimal configuration of ZrO_2 precipitates distributed in clusters in a silica layer, as shown in Fig. 14. The spacing between clusters of ZrO_2 precipitates amounted to 20 μm with a 1.96 μm spacing between ZrO_2 precipitates for consideration of the mechanics of the scale. For the solid silicate phase containing ZrO_2 precipitates, their spacing of 20 μm is considerably less than that found experimentally for the silicate liquid layer of ZrB_2–SiC as reported by Karlsdottir and Halloran.[13] The spacing of ZrO_2 nodules within the liquid boria–silicate melt ranged from 75 to 150 μm, but the spacing may result from Ostwald ripening facilitated by the liquid phase.

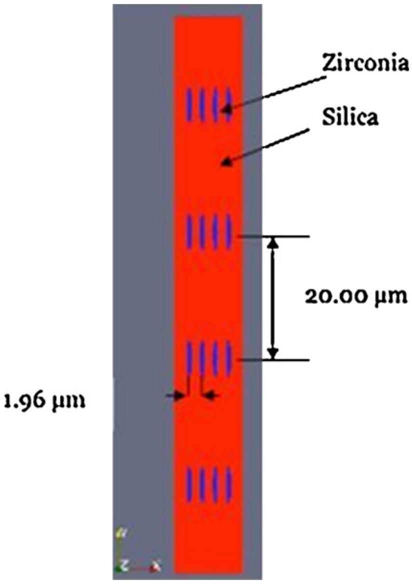

Fig. 14. SiO_2–ZrO_2 layer considering the optimal distribution of ZrO_2 clusters.

5. Discussion

The model of the Zr boride/carbide composite with a $SiO_2/ZrO_2/ZrSi_x$ scale simulates the development of the local strain energetics under a thermal load from 300 to 1700 K. The size of the ZrB_2 and ZrC precipitates creates a maximum strain on the substrate as determined by conventional finite element analysis. The computational analysis using regular finite element analysis determined that the size of the SiO_2 and $ZrSi_x$ precipitates does not appreciably influence the durability of the microstructure. The inconsequential effect of the $ZrSi_x$ precipitates on the strain distribution may result from the metal fraction amounting from 70% to 80% within the composite containing Zr, ZrB_2 and ZrC.

To confirm the microstructural development of the scale on the substrate, a ZrB_2/ZrC/Zr–Si composite was created by reacting a Zr–Si melt with B_4C at approximately 2200 °C, as previously described. A typical acquired microstructure of the matrix consisting of ZrB_2 and ZrC precipitates dispersed in a Zr–Si metal matrix is shown in Fig. 15. The ZrC/ZrB_2/Zr–Si

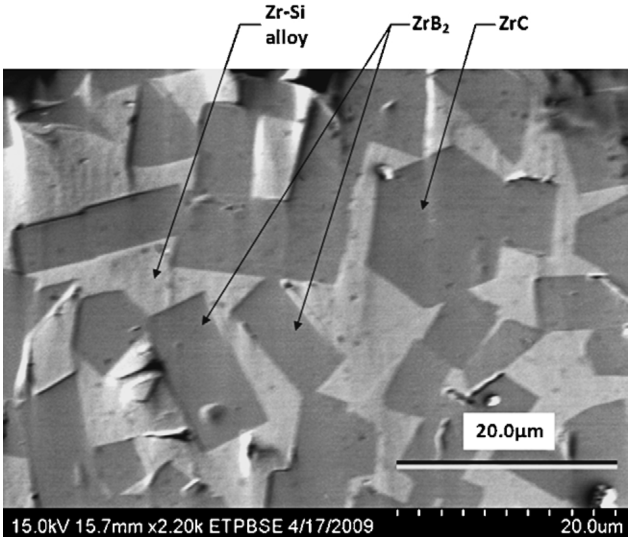

Fig. 15. A scanning electron microscope image of a ZrB_2/ZrC/Zr–Si composite experimentally acquired by reacting a Zr–Si liquid with B_4C.

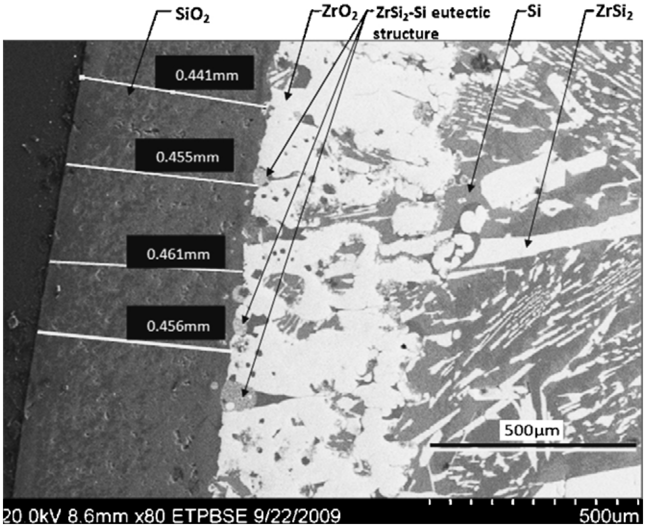

Fig. 16. A microstructure of a SiO_2 layer enveloping a Zr silicide liquid.

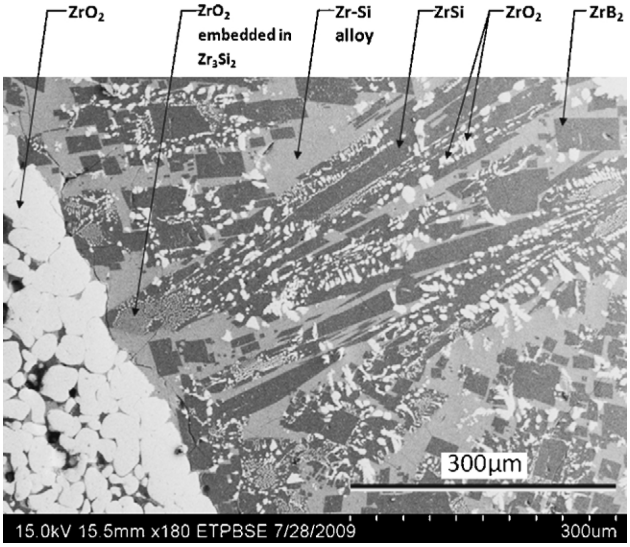

Fig. 17. A microstructure depicting a ZrO_2 layer adjacent to a Zr–Si melt containing ZrB_2.

composite was then heated to 1973 K in air, but disintegrated upon oxidation. The duplex scale consisting of SiO_2 and ZrO_2 layers did not develop adequately to protect the composite.

To determine the efficacy of the silica layer, a $Zr/ZrSi_2$ mixture was placed in a quartz ampoule of 1 mm thickness and then evacuated to create $Zr/ZrSi_2/SiO_2$ couple. The microstructure of the $Zr/ZrSi_2/SiO_2$ couple indicates that the silicate layer protects the couple from oxidation in air, as shown in Fig. 16. The silica layer was less than 1 mm as a result of some vaporization as well as the fluid nature of the quartz wall moving at 1700 °C. Hence, the ZrC/ZrB_2/Zr–Si composite may develop sufficient porosity during ramping toward 1973 K to cause pesting, which can be circumvented with a fluid SiO_2 sealant.

The microstructure of the $Zr/ZrSi_2/SiO_2$ couple also shows that SiO_2, ZrO_2 and a Zr–Si melt developed at 1700 °C, as evident from $ZrSi_2$–Si eutectic structure between the ZrO_2 and SiO_2 phases. Oxygen permeated sufficiently through the SiO_2 layer and reacted with Zr within the silicide melt to form ZrO_2 with adequate growth to encase colonies of $ZrSi_2$–Si eutectic. The original composition of Zr and $ZrSi_2$ mixture amounted to 77 wt% Zr (or 0.51 at% Zr) for a Zr content near the ZrSi compound within the interior of the ampoule. The silicide melt formed during the 44 h anneal because upon cooling the melt solidified without forming ZrSi and precipitated hypo-eutectic $ZrSi_2$ with the $ZrSi_2$–Si eutectic microstructure, as shown in Fig. 16. Although a portion of the Zr content within the silicide melt was consumed by its oxidation to ZrO_2, its formation created three phases consisting of ZrO_2, SiO_2 and Zr–Si(liq). The Zr–Si–O phase diagram at 1973 K indicates that an oxygen potential approximating $10^{-16.5}$ atm was achieved at the $ZrSi_2$–Si structures located along silica interface, as suggested by the silicide melt-silica equilibrium (Fig. 4).

For the encapsulated ZrB_2/ZrC/Zr–Si composite, the microstructure indicates a layer of ZrO_2 grains adjacent to the composite in which ZrB_2 precipitates are evident, as shown in Fig. 17. The ZrO_2 grains may result from their transformations occurring from 1700 °C to room temperature as the zirconia proceeds through the cubic, tetragonal and monoclinic phases with silica located between the grains. In addition, the silica layer acquired from the collapsed quartz wall enveloping the composite limits oxidation. The two-phase equilibrium consisting of silicide and silica, developing with approximately $10^{-16.5}$ atm, does seem to limit the oxygen ingress into the interior. The three-phase equilibria of ZrO_2, ZrSi, and Zr_3Si_2 also suggests that ZrO_2, ZrSi, and Zr_5Si_3 developed or ZrSi–ZrO_2–Zr_5Si_3(O) coexisted at 1700 °C. The oxygen content within a Zr–Si–O system may stabilize the Zr_5Si_3 as Brewer and Kirkorian[41] first reported and later confirmed by Sorrell and McCartney.[42] With ZrSi–ZrO_2–Zr_5Si_3 equilibrium, the oxygen potential of 10^{-18} atm is approached within the interior of the composite. With decreasing temperature, the Zr_5Si_3 becomes unstable and will decompose to Zr_3Si_2, but the Zr_5Si_4 phase was curiously not observed and perhaps the cooling from 1700 °C hampered its precipitation as expected by reaction (3). The microstructure does indicate that ZrB_2 precipitates do not oxidize as a result of the silicide/oxide phases fixing oxygen potentials of $10^{-16.5}$ to 10^{-18} atm.

In summary, the computational modeling suggested that the silicide precipitates along the scale/matrix interface did not cause a significant local strain energy, which probably was minimized by the metal fraction. The simulations using the enriched finite element method did determine that 1.96 µm as the optimal spacing of ZrO_2 precipitates within the silica layer. However, in oxidation of a ZrB_2/ZrC/Zr–Si composite to develop the silica layer, the composite disintegrated upon oxidation because the Zr–Si alloy did not form an adequate silica layer and within it sufficient porosity may have developed. Experiments actually determined that when a silica layer surrounded a silicide or a composite, oxidation was minimized at 1700 °C. Although the oxygen ingress was controlled by the oxygen gradient, the oxygen potentials established on either side of scale by phase equilibria serves to limit oxidation.

6. Conclusions

The study has determined that the size of the ZrB_2 and ZrC precipitates creates a maximum strain on the substrate with the use of conventional finite element analysis, which was applied to create a baseline for the enriched finite element method. The model of the Zr boride/carbide composite with a $SiO_2/ZrO_2/ZrSi_x$ scale simulates the development of the strain energetics under a thermal load from 300 to 1700 K. The computational analysis determined that the size of the SiO_2 and $ZrSi_x$ precipitates does not appreciably influence the durability of the microstructure. A simulated annealing optimization algorithm was also developed for an extended finite element program (called XMicro) with the purpose of optimizing the auto re-meshing of XMicro and thus minimizing its combinatorial selection of a composite's reinforcement architecture. After correcting for the overlapping of ZrO_2 precipitates within a matrix, XMicro determined that 1.96 μm as the optimal spacing of precipitates within a cluster and 20 μm between clusters within a silica matrix of the scale interphase. The $ZrC/ZrB_2/Zr–Si$ composite appear to sustain pesting upon oxidizing in air at 1700 °C. However, a $Zr/ZrSi_2/SiO_2$ couple annealed at 1700 °C for more than 48 h indicates that the silicate layer protects the couple from oxidation. The strategic experimentation determined that porosity developed during oxidation should be incorporated into the simulation of a ceramic composite. The computational mechanics coupled with consideration of the thermodynamic stability of phases for the Zr–Si–O system to set the oxygen potentials between layers can design a scale interphase for an ultrahigh-temperature, ceramic composite system. The processing challenge may be to attain the optimal configuration of the microstructure (e.g., ZrO_2 clusters within a silicate phase).

Acknowledgements

This material is based on research sponsored by the Air Force Research Laboratory, under agreement number FA9550-05-1-0494, through the Air Force Office of Scientific Research (AFOSR) and is gratefully acknowledged with the support of Dr. Joan Fuller of AFOSR. The U.S. Government is authorized to reproduce and distribute reprints for Governmental purposes notwithstanding any copyright notation thereon. The views and conclusions contained herein are those of the authors and should not be interpreted as necessarily representing the official policies or endorsements, either expressed or implied, of the Air Force Research Laboratory or the U.S. Government.

References

1. Rice RW. Review—effects of environment and temperature on ceramic tensile strength-grain size relations. *Journal of Materials Science* 1997;**32**(12):3071–87.
2. Wachtman JB. *Mechanical properties of ceramics*. 1st ed. New York: John Wiley & Sons; 1996.
3. Levine SR, Opila EJ, Halbig MC, Kiser JD, Singh M, Salem J. Evaluation of ultra-high temperature ceramics for aeropropulsion use. *Journal of European Ceramic Society* 2002;**22**:2757–67.
4. Meléndez-Martínez JJ, Domínguez-Rodríguez A, Monteverde F, Melandri C, de Portu G. Characterization and high temperature mechanical properties of zirconium boride-based materials. *Journal of European Ceramic Society* 2002;**22**(14–15):2543–9.
5. Monteverde F, Guicciardi S, Bellosi A. Advances in microstructure and mechanical properties of zirconium diboride based ceramics. *Materials Science and Engineering A* 2003;**346**(1–2):310–9.
6. Loehman R, Corral E, Dumm HP, Kotula P, Tandon R. Ultra high temperature ceramics for hypersonic vehicle applications. *Sandia report*. Albuquerque, NM, 2006.
7. Gridneva IV, Mil'man YuV, Rymashevskii GA, Trefilov VI, Chugunova SI. Effect of temperature on the strength characteristics of zirconium carbide. *Powder Metallurgy and Metal Ceramics* 1976;**15**(8): 638–45.
8. Darolia R, Archbold TF. Plastic deformation of polycrystalline zirconium carbide. *Journal of Materials Science* 1976;**11**(2):283–90.
9. Hinze JW, Tripp WC, Graham HC. The high-temperature oxidation behavior of a HfB_2 + 20 v/o SiC composite. *Journal of Electrochemical Society* 1975;**122**(9):1249–54.
10. Opeka MM, Talmy IG, Zaykoski JA. Oxidation-based materials selection for 2000 °C+ hypersonic aerosurfaces: theoretical considerations and historical experience. *Journal of Materials Science* 2004;**39**(19): 5887–904.
11. Rezaie A, Fahrenholtz WG, Hilmas G. Oxidation of zirconium diboride-silicon carbide at 1500 °C at a low partial pressure of oxygen. *Journal of American Ceramic Society* 2006;**89**(10):3240–5.
12. Phase Equilibria Diagrams Database, version 3.2. *Westerville*, OH: American Ceramic Society, 2008.
13. Karlsdottir SN, Halloran JW. Oxidation of ZrB_2–SiC: influence of SiC content on solid and liquid oxide phase formation. *Journal of American Ceramic Society* 2009;**92**(2):481–6.
14. Muan A. *Electric furnace steelmaking*. Warrendale, PA: Iron and Steel Society; 1985. pp. 357–389.
15. Schnurre SM, Gröbner J, Schmid-Fetzer R. Thermodynamics and phase stability in the Si–O system. *Journal of Non-Crystalline Solids* 2004;**336**(1):1–25.
16. Borodai FYa. Strength of quartz ceramics. *Glass and Ceramics* 1989;**46**(11):463–6.
17. Adams JW, Ruh R, Masdiyasni KS. Young's modulus, flexural strength, and fracture of yttria-stabilized zirconia versus temperature. *Journal of American Ceramic Society* 1997;**80**(4):903–8.
18. Jiménez-Melendo M, Domínguez-Rodríguez A, Bravo-León A. Superplastic flow of fine-grained yttria-stabilized zirconia polycrystals: constitutive equation and deformation mechanisms. *Journal of American Ceramic Society* 1998;**81**(11):2761–76.
19. Jiménez-Melendo M, Domínguez-Rodríguez A. High temperature mechanical characteristics of superplastic yttria-stabilized zirconia. n examination of the flow process. *Acta Materialia* 2000;**48**(12): 3201–10.
20. Owen DM, Chokshi AH. The high temperature mechanical characteristics of superplastic 3 mol% yttria stabilized zirconia. *Acta Materialia* 1998;**46**(2):667–79.
21. Berbon MZ, Langdon TG. An examination of the flow process in superplastic yttria-stabilized tetragonal zirconia. *Acta Materialia* 1999;**47**(8):2485–95.
22. Kajihara K, Yoshizawa Y, Sakuma T. The enhancement of superplastic flow in tetragonal zirconia polycrystals with SiO_2-doping. *Acta Metallurgica et Materialia* 1995;**43**(3):1235–42.
23. Petla H. Computational design of ultra-high temperature ceramic composite materials. Master's Thesis, University of Texas at El Paso, TX, 2008.
24. Wagner C. Diffusion and high temperature oxidation of metals. In: *Atom movements*. Metals Park, OH: American Society of Metals; 1951. pp. 153–173.
25. Yurek GJ. Mechanisms of diffusion-controlled high temperature oxidation of metals. In: Mansfeld F, editor. *Corrosion mechanisms*. New York: Marcel Dekker; 1987. p. 397–446.
26. Kofstad P. *High temperature corrosion*. London: Elsevier Applied Science; 1988. pp. 163–168.

27. Peña M, Ramos C, Bronson A. Phase relations of a silicide/silica reaction couple at 2273 K. *Metallurgical and Materials Transactions B* 1996;**27**(2):271–6.
28. Bale CW, Chartrand P, Degterov SA, Eriksson G, Hack K, Ben Mahfoud R, et al. FactSage thermochemical software and databases. *Calphad* 2002;**26**(2):189–228.
29. Okamoto H. The Zr-Si phase system. *Bulletin of Alloy Phase Diagrams* 1990;**11**(5):513–9.
30. Schmitt N, Burr A, Berthaud Y, Poirier J. Micromechanics applied to the thermal shock behavior of refractory ceramics. *Mechanics of Materials* 2002;**34**:725–47.
31. Zimmermann JW, Hilmas GE, Fahrenholtz WG. Thermal shock resistance of ZrB_2 and ZrB_2–30%SiC. *Materials Chemistry and Physics* 2008;**112**:140–5.
32. Marshall DB, Evans AG. Failure mechanisms in ceramic-fiber/ceramic-matrix composites. *Journal of American Ceramic Society* 1985;**68**:225–31.
33. Umakoshi Y, Nakashima T, Nakano T, Yanagisawa E. Plastic behavior and deformation structure of silicide single crystals with transition metals at high temperatures. *Materials Research Society* 1994;**332**:9–20.
34. Ikarashi Y, Nagai T, Ishizaki K. Fabrication of zirconium silicide intermetallic compounds with 16H-type crystal structure. *Materials Science and Engineering A* 1999;**261**(1–2):38–43.
35. Frommeyer G, Rosenkranz R. Structures and properties of the refractory silicides Ti_5Si_3 and $TiSi_2$ and Ti-Si-(Al) eutectic alloys. In: Senkov ON, Miracle DB, Firstov SA, editors. *Metallic Materials with High Structural Efficiency*. Boston: Kluwer Academic Publishers; 2004. p. 287–308.
36. Frommeyer G, Rosenkranz R, Lüdecke C. Microstructure and properties of the refractory intermetallic Ti_5Si_3 compound and the unidirectionally solidified eutectic Ti-Ti_5Si_3 alloy. *Zeitschrift fur Metallkunde* 1990;**815**: 307–13.
37. Nakano T, Omomoto Y, Hagihara K, Umakoshi Y. Plastic deformation behavior and operative slip systems of ZrSi2 single crystals with C49 type of structure. *Scripta Materialia* 2003;**48**:1307–12.
38. Sukumar N, Chopp DL, Belytschko T. Modeling holes and Inclusions by level sets in the extended finite-element method. *Computer Methods in Applied Mechanics and Engineering* 2001;**190**:6183–200.
39. Belytschko T, Moes N, Usui S, Parimi C. Arbritrary discontinuities in finite elements. *International Journal of Numerical Methods in Engineering* 2001;**50**:993–1013.
40. Johnson WB, Nagelberg AS, Breval. Kinetics of formation of a platelet-reinforced ceramic composite prepared by directed reaction of zirconium with boron carbide. *Journal of American Ceramic Society* 1991;**74**(9):2093–101.
41. Brewer L, Krikorian O. Reactions of refractory silicides with carbon and nitrogen. *Journal of Electrochemical Society* 1956;**103**:701–3.
42. Sorrell CC, McCartney ER. Phase equilibrium in the system zirconium–silicon–oxygen. In: *Proceedings of the 12th Australian Ceramics Conference*. 1986.